

1      Beam Position Reconstruction for the g2p Experiment  
2                          in Hall A at Jefferson Lab

3      Pengjia Zhu<sup>a,\*</sup>, Kalyan Allada<sup>b,g</sup>, Trent Allison<sup>b</sup>, Toby Badman<sup>c</sup>, Alexandre  
4      Camsonne<sup>b</sup>, Jian-ping Chen<sup>b</sup>, Melissa Cummings<sup>d</sup>, Chao Gu<sup>e</sup>, Min Huang<sup>f</sup>,  
5      Jie Liu<sup>e</sup>, John Musson<sup>b</sup>, Karl Slifer<sup>c</sup>, Vincent Sulkosky<sup>e,g</sup>, Yunxiu Ye<sup>a</sup>, Jixie  
6      Zhang<sup>b,e</sup>, Ryan Zielinski<sup>c</sup>

7                          <sup>a</sup>*University of Science and Technology of China, Hefei, Anhui 230026, China*

8                          <sup>b</sup>*Thomas Jefferson National Accelerator Facility, Newport News, VA 23606, USA*

9                          <sup>c</sup>*University of New Hampshire, Durham, NH 03824, USA*

10                        <sup>d</sup>*College of William & Mary, Williamsburg, VA 23187, USA*

11                        <sup>e</sup>*University of Virginia, Charlottesville, VA 22904, USA*

12                        <sup>f</sup>*Duke University, Durham, NC 27708, USA*

13                        <sup>g</sup>*Massachusetts Institute of Technology, MA, 02139, USA*

---

14      **Abstract**

Beam-line equipment was upgraded for experiment E08-027 (g2p) in Hall A at Jefferson Lab. Two beam position monitors (BPMs) were necessary to measure the beam position and angle at the target. A new BPM receiver was designed and built to handle the low beam currents (50-100 nA) used for this experiment. Two new super-harps were installed for calibrating the BPMs. In addition to the existing fast raster system, a slow raster system was installed. Before and during the experiment, these new devices were tested and debugged, and their performance was also evaluated. In order to achieve the required accuracy (1-2 mm in position and 1-2 mrad in angle at the target location), the data of the BPMs and harps were carefully analyzed, as well as reconstructing the beam position and angle event by event at the target location. The calculated beam position will be used in the data analysis to accurately determine the kinematics for each event.

15      **Keywords:** g2p; BPM; raster; beam position

---

\*Corresponding author

Email address: [pzhu@jlab.org](mailto:pzhu@jlab.org), [zhupj55@mail.ustc.edu.cn](mailto:zhupj55@mail.ustc.edu.cn) (Pengjia Zhu)

16     **1. Introduction**

17     A polarized ammonia ( $NH_3$ ) target was used for the first time in Hall A for  
18     the g2p experiment [1]. It operated at a low temperature of 1K and a strong  
19     transverse magnetic field of either 5 T or 2.5 T. A high electron beam current  
20     would cause significant target polarization drop due to target temperature rising  
21     and ionization radiation to the target material [2]. To minimize depolarization,  
22     the beam current was limited to below 100 nA and a raster system was used  
23     to spread the beam spot out to a larger area. The transverse magnetic field  
24     in the target region would cause the beam to be deflected downward when the  
25     beam enters the target region. To compensate for this, two chicane magnets  
26     were placed in front of the target to pre-bend the beam upwards. Due to the  
27     low beam current and tight space limitations after the chicane magnets, the  
28     experimental accuracy goals for the position (1-2 mm) and angle (1-2 mrad) at  
29     the target were challenging to achieve. New beam-line devices and an associated  
30     readout electronics system were designed for the g2p experiment to accomplish  
31     these goals. Design details and the performance of the beam-line devices will  
32     be described in the following sections along with a discussion of a new analysis  
method determine the beam position and direction.

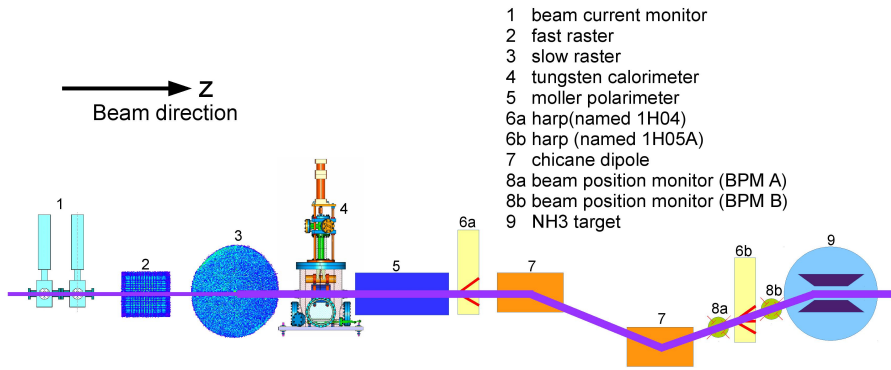


Figure 1: Schematic of beamline components for g2p experiment

34    **2. Beam-line Instrumentation**

35    *2.1. Beam position monitor (BPM)*

36    The scattering angle of the outgoing lepton in deep inelastic scattering, which  
37    is defined with respect to the direction of the incident beam, is an important  
38    variable for obtaining meaningful physics results. Therefore, the position and  
39    direction of the beam, after being bent by the chicane magnetic field and spread  
40    out by the rasters, must be measured precisely. Two BPMs and two harps were  
41    installed for relative and absolute measurements of beam position and direction  
42    near the target, respectively.

43    The BPM consists of four open-ended antennas for detecting the beam po-  
44    sition; the measurement is non-invasive to the beam. The BPM chambers  
45    shown in Fig.2 are part of the beam pipe. The four antennas are attached  
46    to feedthroughs on the interior wall of the pipe at  $90^\circ$  intervals. The BPM

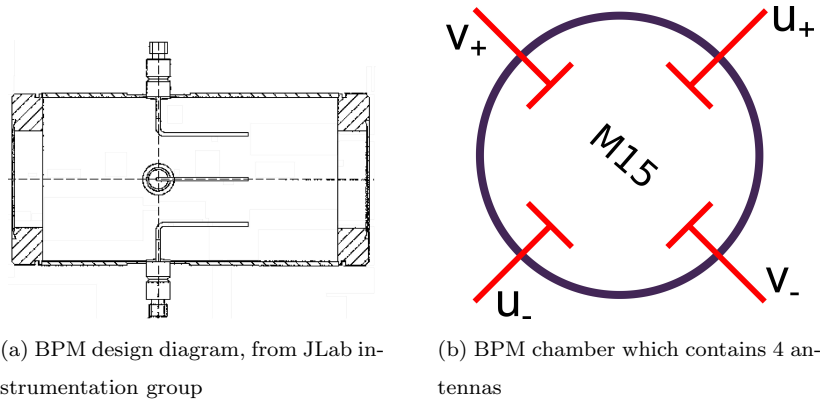


Figure 2: BPM chamber

46  
47    chambers are placed with a  $45^\circ$  rotation (along z) with respect to the global  
48    Hall coordinate. The two pairs of antennas are marked as  $u_+$ ,  $u_-$  and  $v_+$ ,  $v_-$ ,  
49    respectively, which are used to determine beam positions in  $u$  and  $v$  directions.  
50    When the beam passes through the BPM chamber, each antenna receives an  
51    induced signal. The BPM front-end receiver collects and sends the signal to  
52    the regular Hall A DAQ system and another DAQ system designed for parity

53 violation experiments, the HAPPEX system [3]. The new BPM receiver was  
54 designed by the JLab instrumentation group [4] in order to achieve the required  
55 precision at a level of 0.1 mm with a beam current as low as 50 nA. The regular  
56 DAQ system was connected to a 13-bit fastbus ADC (Lecroy ADC 1881) with  
57 an integration time of 50 ns, which was triggered by a scattered electron event.  
58 The HAPPEX system was connected to an 18-bit ADC with an integration  
59 time of 875  $\mu$ s, which was triggered by a beam helicity signal at 1 kHz. The  
60 amplitude,  $A$ , recorded in the ADC has the following relation with the BPM  
61 signal,  $\phi$ :

$$A \propto \phi \cdot 10^{g/20}, \quad (1)$$

62 where  $g$  is the gain of the receiver.

63 The BPM receiver generates a large time delay for the output signals. The  
64 digital filter used in the receiver contributes 1/175 s delay time, which was the  
65 inverse of the bandwidth setting chosen for the filter. There is a  $\sim 4 \mu$ s delay  
66 as a result of finite processing times. The BPM cannot provide event by event  
67 position because of this time delay, due to the 25 kHz fast raster system.

68 Because of the space limitation between the second chicane magnet and the  
69 target, the two BPMs were placed close to each other. One was placed 95.5 cm  
70 upstream of the target while the other was placed 69 cm upstream, making the  
71 distance between them only 26.5 cm. The short distance magnified the position  
72 uncertainty from the BPMs to target.

### 73 *2.2. Super harp*

74 Two super harps were designed and installed in the beam-line, as shown in  
75 Fig.1 (label 6a - 1H04 and 6b - 1H05A), to provide an absolute measurement  
76 of the beam position for calibration of the BPMs. The new harps were able to  
77 work in pulsed beam (1% duty factor) with a current of several  $\mu$ A. A diagram  
78 for the harp is shown in Fig.3, which consists of three wires with a thickness of  
79 50  $\mu$ m, a fork and a controller chassis. The harp chamber is perpendicular to  
80 the beam pipe and connected to the beam pipe as part of the vacuum chamber

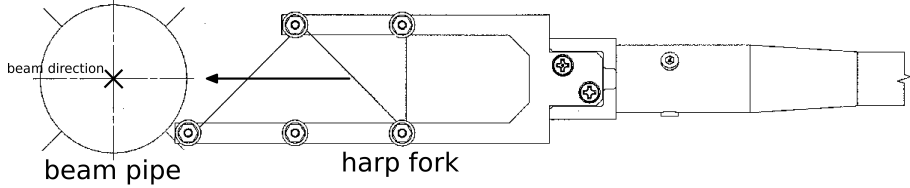


Figure 3: Harp diagram

81 of the beamline. The two harps have different configurations of three wires:  
 82 vertical(|), bank left(\), and bank right(/) for 1H04, and /, |, \ for 1H05. The  
 83 angle of the / or \ wires is 45° relative to the wire dock frame. The wires are  
 84 arranged in a fork (Fig.3) controlled by a step motor [5] which can be moved in  
 85 and out of the beam-line. The harps must be moved out of the beam-line when  
 86 production data is being taken because they are invasive to the beam. The  
 87 original position of the wires was surveyed before the experiment at a precision  
 88 level of 0.1 mm. As the motor driver moved the fork through the beam, each  
 89 wire received a signal, which was recorded for further analysis. The signals  
 90 received from the wire and the step-counters from the motor driver were then  
 91 sent to an amplifier and the DAQ. The amplification and the speed of the motor  
 92 were adjustable for the purpose of optimizing the signals of each scan. Recorded  
 93 data combined with the survey data were used to calculate the absolute beam  
 94 position.

95 The signal from the | wire ( $peak_{|}$ ) was used for getting the  $x$  position ( $x_{harp}$ )  
 96 of the beam, and the signals from the /, \ wires ( $peak_{/}$  and  $peak_{\backslash}$ ) were used  
 97 for getting the  $y$  position ( $y_{harp}$ ):

$$\begin{aligned} x_{harp} &= survey_{|} - peak_{|} \\ y_{harp} &= \frac{1}{2}[(survey_{\backslash} - survey_{/}) - (peak_{\backslash} - peak_{/})] \end{aligned} \quad (2)$$

### 98 2.3. Raster system

99 In order to minimize the depolarization, avoid damage to the target material  
 100 from radiation, and reduce systematic error for the polarization measurement by  
 101 NMR (The polarization of the  $NH_3$  target was measured by using a NMR coil

102 which was placed inside the target cell [6]. The non-uniformity of depolarization  
 103 could reduce the precision of the NMR measurement due to the measurement  
 104 being an average over the target), two raster systems were installed at  $\sim 17$  m  
 105 upstream of the target, as shown in Fig.1 (labels 2 and 3 for fast and slow rasters,  
 106 respectively). Both the fast and slow rasters consist of two dipole magnets. The  
 107 same triangular waveforms with frequency of 25 kHz were used to drive the  
 108 magnet coils of the fast raster to move the beam in x and y directions, forming  
 a rectangular pattern of about 2 mm  $\times$  2 mm, as shown in Fig.4.

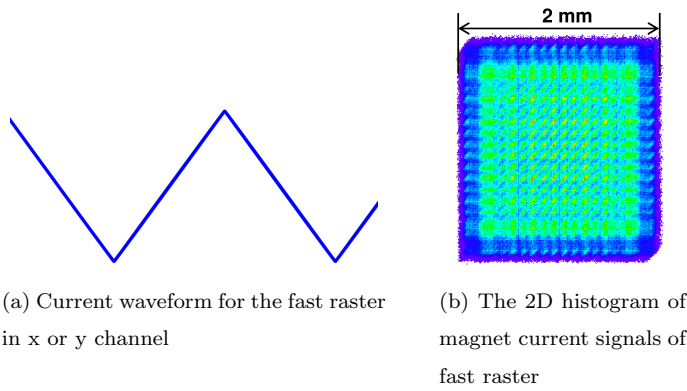


Figure 4: Fast raster pattern

109  
 110 A dual-channel function-generator<sup>1</sup> was used to generate two independent  
 111 waveforms to drive the magnet coils of the slow raster. The waveforms for the  
 112  $x$  and  $y$  directions are:

$$\begin{aligned}
 x &= A_x t^{1/2} \sin(\omega t), \\
 y &= A_y (t + t_0)^{1/2} \sin(\omega t + \phi),
 \end{aligned} \tag{3}$$

113 where the  $A_x$  and  $A_y$  are the maximum amplitude,  $t_0$  and  $\phi$  are the AM and  
 114 sin phase difference between  $x$  and  $y$  waveform, respectively. Both of them

---

<sup>1</sup>agilent 33522A function generator, <http://www.home.agilent.com/en/pd-1871286-pn-33522A/function-arbitrary-waveform-generator-30-mhz>

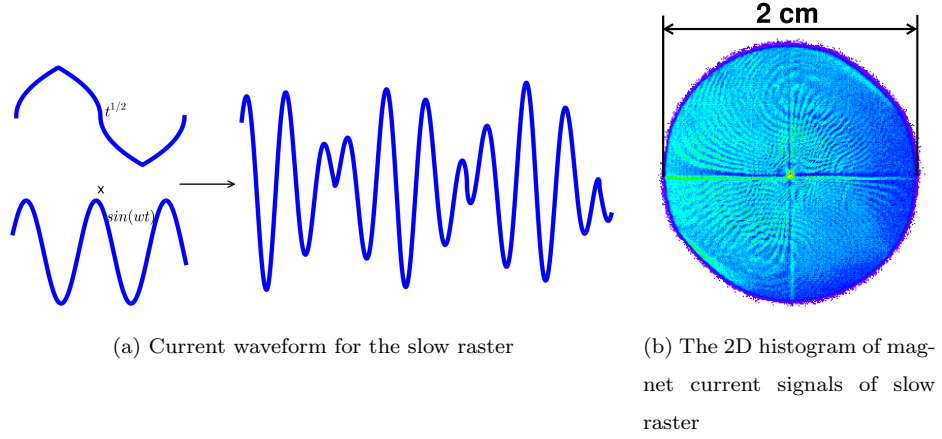


Figure 5: Slow raster pattern

115 are sine functions modulated by a function  $t^{1/2}$  in order to generate a uniform  
 116 circular pattern [7], as shown in Fig.5. The frequencies of the  $x$  and  $y$  waveforms  
 117 kept same:  $\omega = 99.412$  Hz. In order to cycle the amplitude modulation (AM)  
 118 function, four piece-wise functions are combined together. The first term is  $t^{1/2}$ ,  
 119 and the second term is  $period - t^{1/2}$ , and so on for the third and fourth terms.  
 The cycled function has the frequency of 30 Hz.

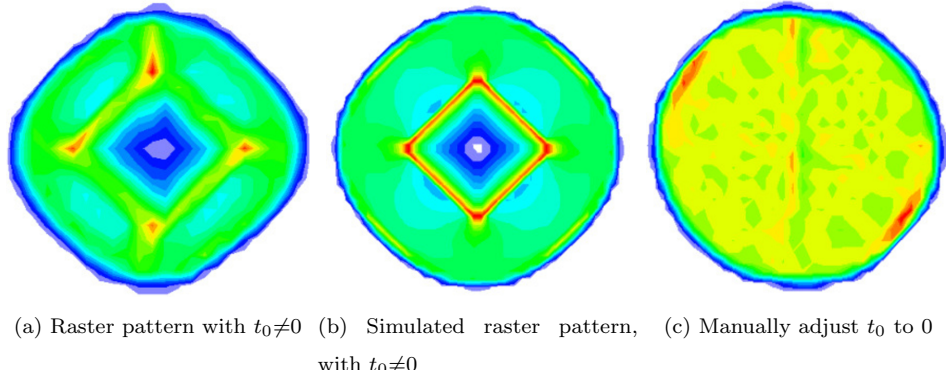


Figure 6: None-zero  $t_0$  caused slow raster non-uniformity, (a) and (c) are from the data recorded in the ADC, (b) is simulated.

121     The  $\phi$  was locked to  $\frac{\pi}{2}$  by the function generator, while the  $t_0$  was manually  
 122     fixed to 0. Non-zero  $t_0$  could cause a non-uniformity pattern, as shown in  
 123     Fig.6(a), which would cause non-uniformity beam distribution. A simulation  
 124     was reproduced the non-uniformity by setting the  $t_0$  to non-zero, as shown  
 125     in Fig.6(b). The  $t_0$  was carefully adjusted and minimized before production  
 126     data taking to avoid the non-uniformity. The pattern of the spread beam was  
 127     relatively uniform after this adjustment during the experiment, as shown in  
 128     Fig.6(c).

129     **3. Data analysis**

130     *3.1. Harp scans for measuring absolute beam position*

An example of a harp scan result is shown in Fig.7. There are three groups of

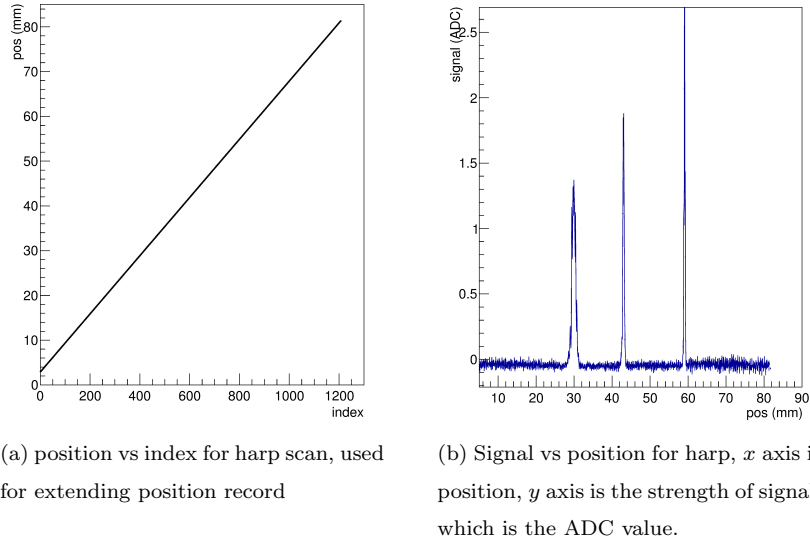


Figure 7: 1H05A harp scan data

131  
 132     recorded data for each harp scan, which are “index”, “position”, and “signal”.  
 133     The index is related to the moving steps of the fork during the scan. Each  
 134     step of the index increases by 0.008-0.07 mm depending on the speed of the  
 135     motor driver [5]. The position is the wire location for each index. The testing

136 results show a good linear relation between the position and the index as shown  
137 in Fig.7(a), because the motor speed is uniform. The line is the fitted result  
138 with  $pos = a * index + b$ . According to this linear relation, interpolation or  
139 extrapolation can be applied when a few data points are missing, in some cases.  
140 The strength of signal vs. position is plotted in Fig.7(b). Each peak represents  
141 the location when one of the three wires passed through the beam.

142 The positions measured by the two harps were used for calibrating the beam  
143 positions in the two BPMs. When the chicane magnets were on, beam did not  
144 pass straight through from the first harp to the second harp. BPM calibrations  
145 using two harps were only possible when the chicane magnets were off, i.e. in the  
146 straight-through settings. Since the BPM was calibrated in the local coordinate  
147 system, the calibration constants were independent from the settings of other  
148 instruments. To make sure that the calibration constants for the BPMs were  
149 still valid during the non-straight-through settings, the settings for the BPM  
150 receiver were kept the same as in the straight-through settings during production  
151 running.

152 The scan data from the harps were not reliable when the current of CW  
153 beam (100% duty factor) was lower than 100 nA due to the low signal-to-noise  
154 ratio. The harp scans were taken in pulsed mode at a current of a few  $\mu$ A, while  
155 the BPMs were used for production data taking in CW mode at a beam current  
156 of 50-100 nA. For a BPM calibration run, a harp scan was done first in pulsed  
157 mode, then a DAQ run was taken immediately to record the ADC value in CW  
158 mode without changing the beam position. The harp scan was then taken again  
159 in the pulsed mode to double check the beam position. The harp scan data was  
160 discarded and the scan was taken again if the beam position changed.

161 *3.2. BPM data analysis and calibration*

162 The traditional difference-over-sum ( $\Delta/\Sigma$ ) method of calculating the beam  
163 position has the non-linearity effect at the position far away from the center of  
164 the beam pipe [8]. It is necessary to correct the equation of  $\Delta/\Sigma$  since we have a  
165 slow raster with a large size of  $\sim 2$  cm. With the assumption of an infinitely long

<sup>166</sup> chamber and neglecting the antenna influence on the electric field inside the  
<sup>167</sup> chamber, the signal from each antenna excited by the beam can be calculated  
<sup>168</sup> via image charge method (Fig. 8) [9, 10] :

$$\phi_i = \phi_0 I \frac{R^2 - \rho^2}{R^2 + \rho^2 - 2R\rho\cos(\theta_i - \theta_0)}, \quad (4)$$

<sup>169</sup> where  $\phi_i$  is the signal received in the antenna, and  $i$  is  $u_+$ ,  $u_-$ ,  $v_+$  and  $v_-$ ,  
<sup>170</sup> respectively,  $\phi_0$  is a constant related to the geometry of the BPM-chamber and  
<sup>171</sup> the output resistance,  $I$  is the beam current,  $R$  is the radius of the BPM vacuum  
<sup>172</sup> chamber,  $\rho$  is the radial position of the beam, and  $\theta_i - \theta_0$  is the angle difference  
 between the antenna and the beam in the polar coordinate .

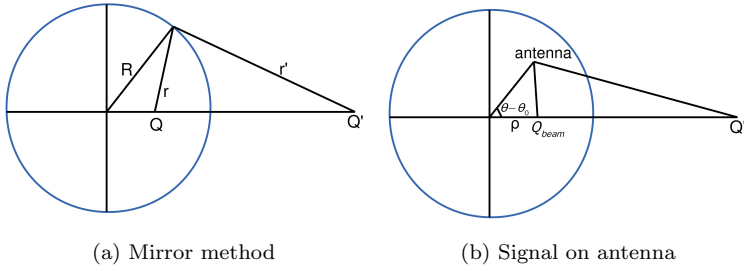


Figure 8: Signal for each antenna of BPM

<sup>173</sup>  
<sup>174</sup> In order to extract the beam position information, and eliminate the depen-  
<sup>175</sup> dence on the beam current in equation (4), the  $\Delta/\Sigma$  method is used as follows:

$$D_U = \frac{\phi_{U+} - \phi_{U-}}{\phi_{U+} + \phi_{U-}}, \quad (5)$$

<sup>176</sup> where  $\underline{U}$  denotes  $u$  and  $v$ . Substituting equation (4) into equation (5), it can be  
<sup>177</sup> rewritten as follows:

$$D_U = \frac{\phi_{U+} - \phi_{U-}}{\phi_{U+} + \phi_{U-}} = \frac{2}{R} \frac{\rho\cos(\theta - \theta_0)}{1 + \frac{\rho^2}{R^2}} = \frac{2}{R} \frac{U}{1 + \frac{\rho^2}{R^2}}, \quad (6)$$

<sup>178</sup> where  $\rho^2 = u^2 + v^2$ . When  $u^2 + v^2 \ll R^2$ , equation (6) is simplified as:

$$U \approx \frac{R}{2} D_U = \frac{R}{2} \frac{\phi_{U+} - \phi_{U-}}{\phi_{U+} + \phi_{U-}}. \quad (7)$$

179 Equation (7) can be used in the simple case when the beam is near the center  
 180 of the beam pipe. When the beam is far from the center, equation (7) is no  
 181 longer valid. For the g2p experiment, the beam was rastered to have a diameter  
 182 of about 2 cm at the target. From equation (6) the beam position is calculated  
 183 as:

$$U = RD_U \left( \frac{1}{D_u^2 + D_v^2} - \frac{1}{\sqrt{D_u^2 + D_v^2}} \sqrt{\frac{1}{D_u^2 + D_v^2} - 1} \right). \quad (8)$$

184 To verify this correction equation, a simulation was performed. First, a  
 185 set of position data were generated (Fig.9(a)), and the designed radius of the  
 186 BPM chamber was used for  $R$ . Using equation (4) to get the signal for each  
 187 antenna and ignoring  $\phi_0$  and  $I$ , equations (8) and (7) were used to calculate  
 188 the beam position for comparison. The results are shown in Fig.9(b) and 9(c),  
 respectively.

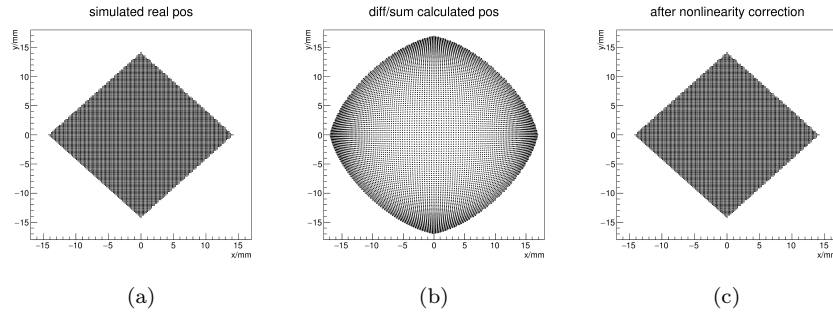


Figure 9: Comparing the calculated results using equation (7) and (8) with simulated position.  
 (a) Simulated position; (b) The calculated result with equation (7), (c) The calculated result  
 with equation (8).

189  
 190 The correction equation is also tested by using the experiment data and the  
 191 bench test data. Fig.10(a) shows the comparison between the position calcu-  
 192 lated from the correction equation (8) and the one from the  $\Delta/\Sigma$  equation (7).  
 193 Fig.10(b) shows the comparison with the real beam position from the bench test  
 194 data. In this way the method using equation (8) can correct the non-linearity  
 195 effect caused by the  $\Delta/\Sigma$  method. The handling of the BPM information which

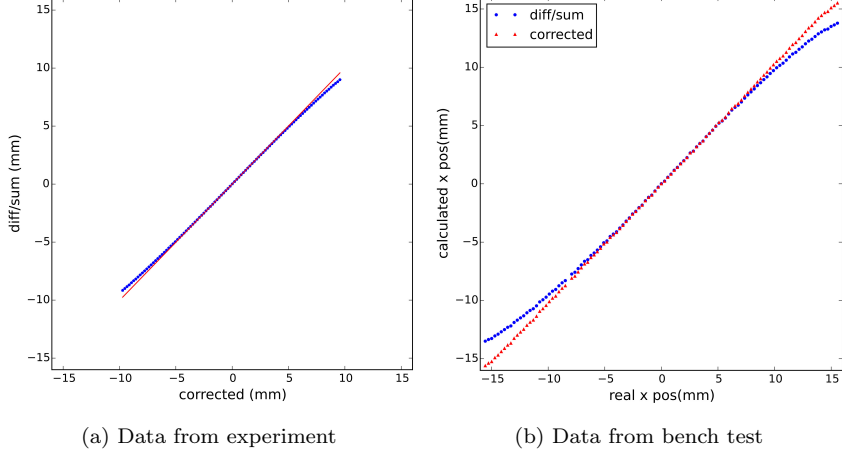


Figure 10: BPM non-linearity correction. (a) Comparison between the position calculated from  $\Delta/\Sigma$  equation (7) (y axis) and the one from correction equation (8) (x axis). Red solid line is a reference line came from linear fit of the center points. Data is collected from the experiment. (b) Comparison between the  $\Delta/\Sigma$  equation (7) and the correction equation (8) using the bench test data. The x axis is the real beam position. The red triangles are the positions calculated from correction equation (8). The blue circles are the positions calculated from  $\Delta/\Sigma$  equation (7) .

196 only used for the center beam position (discussed in chapter 3.4) also reduced  
197 this non-linearity effect.

198 The final information recorded in the data-stream was designed to have a  
199 linear response with the raw signal in the 50-100nA current range. The  $\phi_i$  in  
200 equation (6) can be rewritten as:

$$\phi_i = a_i(A_i - A_{i-ped} + b_i), \quad (9)$$

201 where  $A_i$  and  $A_{i-ped}$  are the recorded ADC value and pedestal value, and  $a_i$  and  
202  $b_i$  are the slope and intercept of the relationship between  $\phi_i$  and  $A_i - A_{i-ped}$ .  
203 Equation (7) can be rewritten as:

$$D_U = \frac{(A_{U+} - A_{U+-ped} + b_{U+}) - h_U(A_{U-} - A_{U--ped} + b_{U-})}{(A_{U+} - A_{U+-ped} + b_{U+}) + h_U(A_{U-} - A_{U--ped} + b_{U-})}, \quad (10)$$

204 where  $h_U = a_{U-}/a_{U+}$ , which is related to the ratio of the signals from the  $U_+$   
 205 and  $U_-$  antennas and the gain settings of the two channels.

206 Combining the equations (9) and (4), the calibration constant  $b_i$  was ob-  
 207 tained by taking the linear fit between the ADC values of BPM and the beam  
 208 current:  $I \propto (A_i - A_{i-ped} + b_i)$ . Besides, the linear fit used a group of runs which  
 had the same beam position but different beam current. Figure 11 shows the

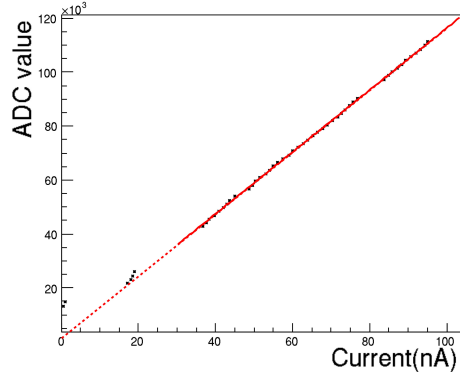


Figure 11: ADC value of BPM raw signal ( $A - A_{ped}$ ) V.S. current

209  
 210  $A_i - A_{i-ped}$  versus the beam current. It shows that the ADC values were linear  
 211 with beam current in the considering current range of 50-100 nA. The intercept  
 212 from the linear fit of Fig.11 is the value  $b_i$ .

213 By transporting the position  $x_{harp}$  and  $y_{harp}$  in equation (2) from two harps  
 214 to the BPM local coordinate  $u_{harp}$  and  $v_{harp}$ , a fit between the BPM data  $U$   
 215 and the harp data  $U_{harp}$  determined three calibration constants  $c_0$ ,  $c_1$  and  $c_2$ :

$$U_{harp} = U_c = c_0 + c_1 u + c_2 v, \quad (11)$$

216 where  $U_c$  is the calibrated BPM position. It was converted to Hall coordinate  $X_c$   
 217 for further transporting to the target location. An calibration example is shown  
 218 in Fig. 12. The asterisks in Fig. 12 represent  $U_{harp}$ , and the dots represent  $U$ .

219 In order to reduce the noise and improve the resolution during data analysis,  
 220 a software filter was applied. Since the 18 bit ADC was triggered by the helicity  
 221 signal with a fixed frequency, it could be regarded as a sampling ADC. Fig.13

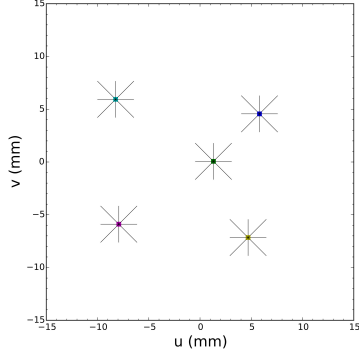


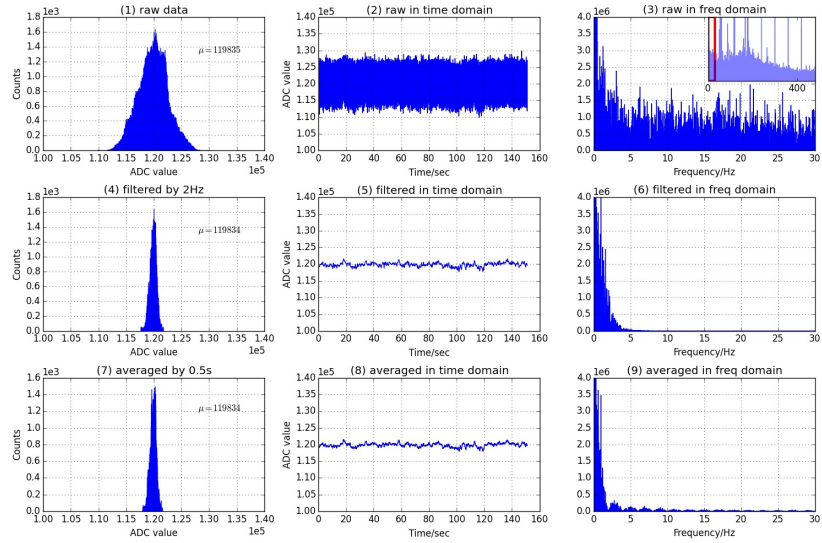
Figure 12: Harp scan data combined with BPM data, the asterisks are the positions from harp, while the dots are from BPM.

222 shows the signal dealt with a 2 Hz low pass filter. Three plots at the bottom of  
 223 Fig. 13 (a,b) are the averaged signal used for comparing with the filtered signal.  
 224 The results show that the 2 Hz filter and the 0.5 s average are consistent within  
 225 the required precision. The filter also erases the beam displacement caused by  
 226 the rasters, which is necessary to extract the position of the beam center.

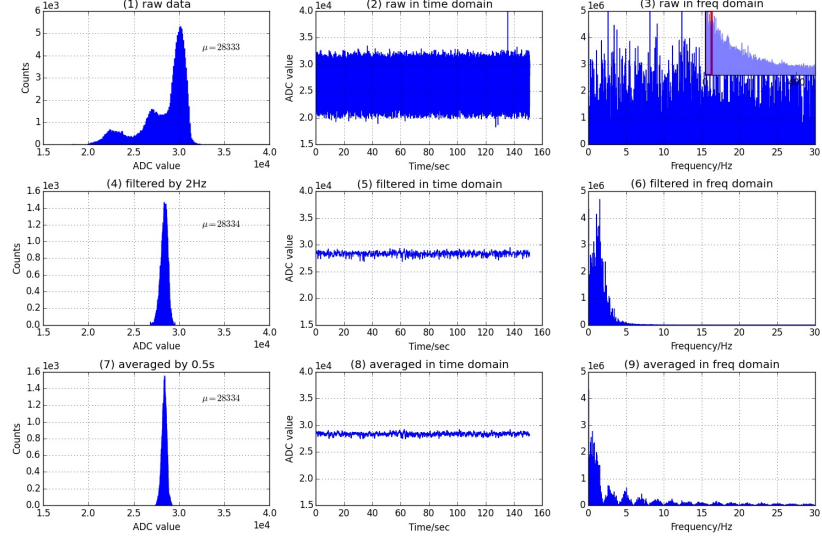
227 *3.3. Beam position reconstruction at the target*

228 It is easy to transport the position from the BPMs to the target by using a  
 229 linear transportation method for the straight through setting. For the settings  
 230 with a transverse magnetic field at the target, the linear transportation method  
 231 cannot be used since the beam is bent near the target. A target magnet field  
 232 map [11] was generated from the TOSCA model. To test the accuracy of the  
 233 TOSCA model, the target magnet field was measured before the experiment  
 234 [12, 13]. The position and angle at target were calculated in terms of the  
 235 positions at BPMA and BPMB, together with the magnet field information.  
 236 Fits were used to speed up the calculation. To do this, a full simulation was  
 237 taken by generating thousands of trajectories with different initial positions and  
 238 angles. The fits were compared with the full simulation and they are consistent  
 239 with negligible difference. Fig. 14 shows the trajectories from the simulation.

240 The fitted transport functions were only used to transport the beam center



(a) Normal run with beam



(b) Pedestal run without beam

Figure 13: Software filter applied to BPM signal. (a) is the signal with beam, (b) is the pedestal signal without beam. (1,2,3) in (a,b) are the raw signal without applying the filter, (4,5,6) are applied a 2Hz finite-impulse-response filter with 4th order. (7,8,9) are averaged with 0.5 s. (1,4,7) are the 1-D histogram of the recorded signal, (2,5,8) are the signal in time domain, (3,6,9) are in frequency domain. Note all of the plots in (a) is for a single signal, same as in (b).

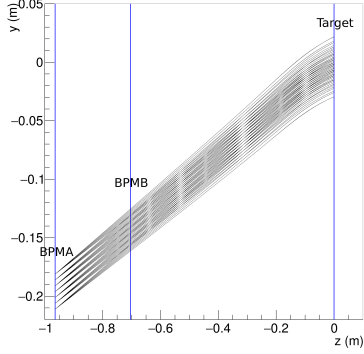


Figure 14: Transporting beam position from BPM to target with transverse target magnet field. Trajectories are from simulation. Blue lines show the  $z$  position of BPMA, BPMB and target.  $y$  and  $z$  are in global Hall coordinate.

position from the two BPMs to the target by applying the 2 Hz filter, which filtered out the fast raster and slow raster motion to keep only the beam center position. The transported position were expressed as  $X_{center}$ .

#### 3.4. Determining the beam position event-by-event

The readout of the magnet current for the two rasters was connected to a series of ADCs. Two scintillator planes in the HRS form a DAQ trigger. This pulse signal triggered the ADC to record the raster magnet current for each event. The information from the rasters and the BPMs was combined to provide the beam position event-by-event. The position at the target was determined as:

$$X = X_{center} + X_{fstraster} + X_{slraster}, \quad (12)$$

where  $X_{fstraster}$  and  $X_{slraster}$  were the position displaced by the fast raster and slow raster, respectively, which were converted from the current values of the two raster magnets. The calibration of the conversion factors between the magnet current of the rasters and the displaced position will be discussed in the next subsection. An example of reconstructed beam position is shown in Fig. 15.

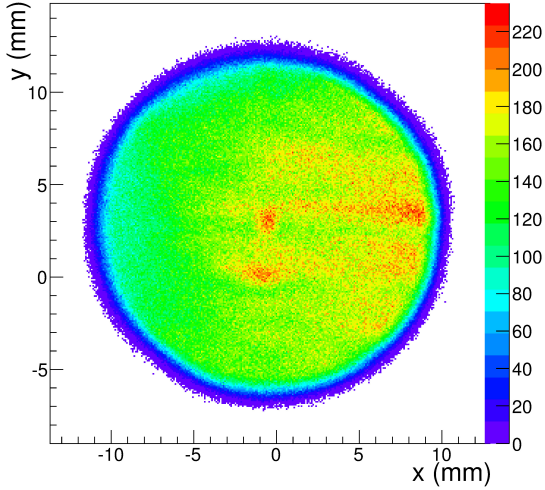


Figure 15: Reconstructed beam position at the target

*3.4.1. Conversion factor for the slow raster*

Two methods were used to calibrate the conversion factor for the slow raster. The first method used the calibrated BPM information, i.e., comparing the raster magnet current with the beam shape shown in the ADC of the BPMs. Several calibrations were taken during different run periods at a beam current of 100nA using different values of the raster magnet current, as shown in Fig.16(a).

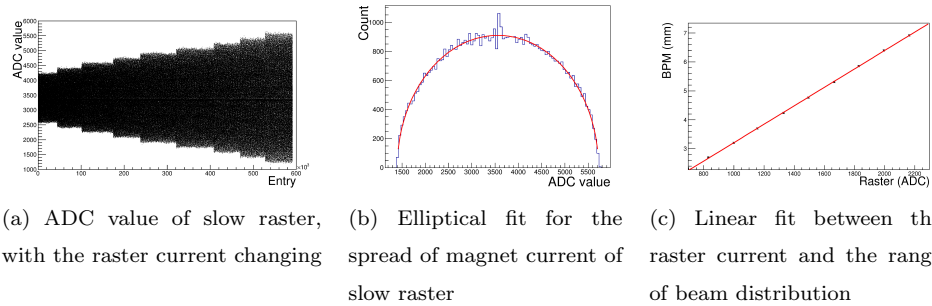


Figure 16: Converting the raster current to beam position shift

263

264 The range of the beam distribution at the target was calculated from the

265 ranges at the two BPMs without applying the filter, using the transport functions  
 266 fitted previously. The range of the beam distribution at the two BPMs  
 267 and the amplitude of the raster current were calculated from elliptical fits. An  
 268 example of the fit is shown in Fig.16(b). Figure 16(c) shows a linear fit between  
 269 the raster current and the range of the beam distribution at the target. The x  
 270 axis in Fig.16(c) is the magnet current of the raster, and the y axis is the range  
 271 of the beam distribution obtained from the BPMs.

272 The second method for calibrating the conversion factor used a target called  
 273 “carbon hole” as shown in Fig.17(a). Scattered electrons were used as the

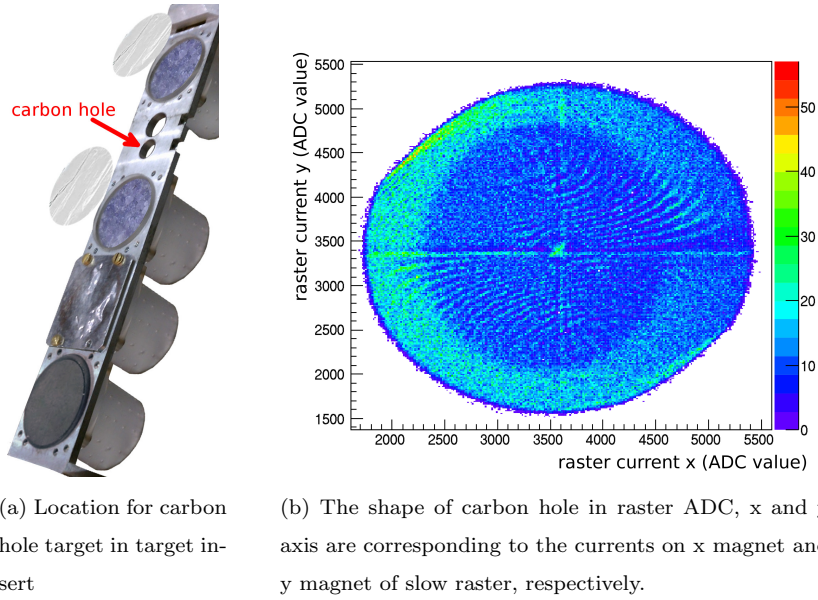


Figure 17: Carbon hole method to calibrate raster

274 trigger for recording the raster magnet current. Since the density of the target  
 275 frame was much higher than that of the “hole”, which was submerged in liquid  
 276 helium, the density of events triggered from the target frame was much higher  
 277 than that of the hole itself. Recorded values reveal a hole shape as shown in  
 278 Fig.17(b). The size of the carbon hole was surveyed before the experiment, and  
 279 a fit program was used to extract the radius of the recorded hole shape for that  
 280 raster current. The conversion factor  $F$  was then calculated as the ratio of the

281 size of the carbon hole  $S_{hole}$  and the radius of the hole shape  $R_{hole}$  in the ADC:

$$F = \frac{S_{hole}}{2 * R_{hole}}. \quad (13)$$

282 *3.4.2. Conversion factor for the fast raster*

283 The conversion for the fast raster was the same as for the slow raster. The  
284 low pass filter for the BPM was set to a higher value than the frequency of the  
285 fast raster to see the beam shape at the BPM formed by the fast raster. For a  
286 higher frequency filter, a larger beam current was needed to get a clear pattern.  
287 The beam current chosen for calibrating the fast raster was near 300 nA, which  
288 was the safety limit for the target. The beam shape formed by the fast raster  
is shown in Fig.18.

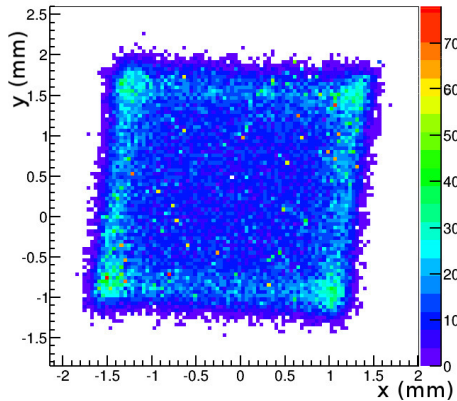


Figure 18: Beam shape formed by the fast raster at the BPM A location, the unit is millimeter

289

290 **4. Uncertainty**

291 The uncertainty of the final beam position at the target for each event con-  
292 tains several contributions:

- 293 • The first part comes from the uncertainty of the calibration constant. It  
294 includes the BPM resolution for the DAQ runs used for the calibration,  
295 the uncertainty of the harp data corresponding to each calibration, and

296 the survey uncertainties for the BPMs and harps. It contributes about 0.7  
297 mm for the uncertainty of the position and 0.7 mrad for the uncertainty  
298 of the angle.

- 299 • The uncertainty on the pedestal is the largest uncertainty for the beam  
300 position measurement, contributing about 0.7~1.5 mm to the uncertainty  
301 of the position and 0.7~1.5 mrad to the uncertainty of the angle.  
302 • The uncertainties from the BPM survey need to be included, since the  
303 production data and the calibration data were taken at different beamline  
304 settings when the equipment was moved. They contribute 0.5 mm to the  
305 uncertainty of the position.  
306 • The uncertainty from the magnetic field map of the target was considered  
307 for the settings with the target magnet field.  
308 • The uncertainties due to the size conversion of the rasters were also in-  
309 cluded.

310 The position uncertainty was magnified by a factor of 5 at the target because of  
311 the short distance between the two BPMs. For example, in the straight through  
312 setting, if the uncertainty at BPM A is 0.2 mm, and at BPM B is 0.27 mm,  
313 the uncertainty at the target is 1.1 mm for position and 1.3 mrad for angle.  
314 The uncertainty for the position at the target was around 1~2 mm, while the  
315 uncertainty for the angle was 1~2 mrad.

## 316 5. Summary

317 JLab g2p experiment used a transversely polarized  $NH_3$  target for the first  
318 time in Hall A. It put a limit of below 100 nA on the electron beam current and  
319 required a slow raster to spread beam to a large area. Two chicane magnets were  
320 used to compensate the strong transverse magnetic field. Beam-line equipment,  
321 including the BPMs, harps and associated readout system, were upgraded to  
322 allow precision measurements of the beam position at low current (50-100 nA).

323 A software filter was used to reduce noise of the BPMs. A correction equation  
324 was used to compensate the non-linearity caused by the  $\Delta/\Sigma$  equation. The  
325 harp data and the linear fit between the bpm signal and the beam current  
326 were used to extract the calibration constant of the BPM. To account for the  
327 strong target magnetic field effect, transport functions were fitted to transport  
328 the beam position from the BPMs to the target. The beam position in the  
329 x-y plane and the angle at the target location are extracted event-by-event by  
330 combining information from the BPMs and the signals from the rasters. The  
331 performance of the new devices (BPMs, harps and slow rasters) were presented  
332 along with an analysis of systematic uncertainties.

333 **Acknowledgments**

334 This work was supported by DOE contract DE-AC05-84ER40150 under  
335 which the Southeastern Universities Research Association (SURA) operates the  
336 Thomas Jefferson National Accelerator Facility, and by the National Natural  
337 Science Foundation of China (11135002, 11275083), the Natural Science Foun-  
338 dation of Anhui Education Committee (KJ2012B179).

339 **Reference**

- 340 [1] A. Camsonne, J. P. Chen, D. Crabb and K. Slifer, spokesperson, JLab  
341 E08-027 (g2p) experiment. 1
- 342 [2] D. G. Crabb, W. Meyer, Solid polarized targets for nuclear and particle  
343 physics experiments, *Annu. Rev. Nucl. Part. Sci.* 47 (1997) 67–109. 1
- 344 [3] R. Michaels, Precision Integrating HAPPEX ADC, JLab Technical report  
345 (unpublished).
- 346 URL [http://hallaweb.jlab.org/parity/prex/adc18/prex\\_adc18\\_](http://hallaweb.jlab.org/parity/prex/adc18/prex_adc18_spec.ps)  
347 `spec.ps` 2.1
- 348 [4] J. Musson, Functional Description of Algorithms Used in Digital Receivers,  
349 JLab Technical report No. JLAB-TN-14-028. 2.1

- 350 [5] C. Yan and et al., Superharp - A wire scanner with absolute position read-  
351 out for beam energy measurement at CEBAF, Nuclear Instruments and  
352 Methods in Physics Research A 365 (1995) 261–267. 2.2, 3.1
- 353 [6] J. Pierce, J. Maxwell, T. Badman, J. Brock, C. Carlin, D. Crabb, D. Day,  
354 C. Keith, N. Kvaltine, D. Meekins, J. Mulholland, J. Shields, K. Slifer,  
355 Dynamically polarized target for the and experiments at jefferson lab,  
356 Nuclear Instruments and Methods in Physics Research Section A: Acceler-  
357 ators, Spectrometers, Detectors and Associated Equipment 738 (0) (2014)  
358 54 – 60. doi:<http://dx.doi.org/10.1016/j.nima.2013.12.016>.  
359 URL [http://www.sciencedirect.com/science/article/pii/  
360 S0168900213016999](http://www.sciencedirect.com/science/article/pii/S0168900213016999) 2.3
- 361 [7] C. Yan, Hall C Polarized Target Raster System Upgrade, JLab Technical  
362 report (unpublished).  
363 URL [https://www.jlab.org/Hall-C/talks/01\\_06\\_05/yan.pdf](https://www.jlab.org/Hall-C/talks/01_06_05/yan.pdf) 2.3
- 364 [8] W. Barry, A general analysis of thin wire pickups for high fre-  
365 quency beam position monitors, Nuclear Instruments and Meth-  
366 ods in Physics Research Section A: Accelerators, Spectrometers,  
367 Detectors and Associated Equipment 301 (3) (1991) 407 – 416.  
368 doi:[http://dx.doi.org/10.1016/0168-9002\(91\)90004-A](http://dx.doi.org/10.1016/0168-9002(91)90004-A).  
369 URL [http://www.sciencedirect.com/science/article/pii/  
370 016890029190004A](http://www.sciencedirect.com/science/article/pii/016890029190004A) 3.2
- 371 [9] C.R.Carman, J. L. Pellegrin, The beam positions of the spear storage ring,  
372 SLAC-PUB-1227. 3.2
- 373 [10] P.Poit, Evaluation and correction of nonlinear effects in fnpl beam position  
374 monitors, FNPL Technical report No.Beams-doc-1894-v1.  
375 URL [http://beamdocs.fnal.gov/AD-public/DocDB>ShowDocument?  
376 docid=1894](http://beamdocs.fnal.gov/AD-public/DocDB>ShowDocument?docid=1894) 3.2
- 377 [11] R. Wines, private communication. 3.3

- 378 [12] J. Liu, Magnetic field mapping on a translation table, JLab Technical  
379 report, E08-027 Collaboration (unpublished).
- 380 URL [http://hallaweb.jlab.org/experiment/g2p/collaborators/jie/2011\\_10\\_05\\_fieldmap\\_report/Target\\_Field\\_Map\\_Report.pdf](http://hallaweb.jlab.org/experiment/g2p/collaborators/jie/2011_10_05_fieldmap_report/Target_Field_Map_Report.pdf) 3.3
- 382 [13] C. Gu, Target field mapping and uncertainty estimation, JLab Technical  
383 report, E08-027 Collaboration (unpublished).
- 384 URL [https://hallaweb.jlab.org/experiment/g2p/collaborators/chao/technotes/Chao\\_TechNote\\_TargetField.pdf](https://hallaweb.jlab.org/experiment/g2p/collaborators/chao/technotes/Chao_TechNote_TargetField.pdf) 3.3